

CFD–DEM simulation of biomass gasification with steam in a fluidized bed reactor



Xiaoke Ku*, Tian Li, Terese Løvås

Department of Energy and Process Engineering, Norwegian University of Science and Technology (NTNU), 7491 Trondheim, Norway

HIGHLIGHTS

- A CFD–DEM model is developed to simulate the biomass gasification in a FB reactor.
- Higher temperatures are favorable for the products in endothermic reactions.
- H₂ and CO₂ concentrations increase with the increase of steam/biomass mass ratio.
- Carbon conversion decreases as the height of fuel injection point increases.
- The calculated results compare well with the experimental data.

ARTICLE INFO

Article history:

Received 4 June 2014

Received in revised form

18 August 2014

Accepted 20 August 2014

Available online 27 August 2014

Keywords:

CFD–DEM

Biomass gasification

Steam

Fluidized bed reactor

Syngas

Carbon conversion

ABSTRACT

A comprehensive CFD–DEM numerical model has been developed to simulate the biomass gasification process in a fluidized bed reactor. The methodology is based on an Eulerian–Lagrangian concept, which uses an Eulerian method for gas phase and a discrete element method (DEM) for particle phase. Each particle is individually tracked and associated with multiple physical (size, density, composition, and temperature) and thermo-chemical (reactive or inert) properties. Particle collisions, hydrodynamics of dense gas–particle flow in fluidized beds, turbulence, heat and mass transfer, radiation, particle shrinkage, pyrolysis, and homogeneous and heterogeneous chemical reactions are all considered during biomass gasification with steam. A sensitivity analysis is performed to test the integrated model's response to variations in three different operating parameters (reactor temperature, steam/biomass mass ratio, and biomass injection position). Simulation results are analyzed both qualitatively and quantitatively in terms of particle flow pattern, particle mixing and entrainment, bed pressure drop, product gas composition, and carbon conversion. Results show that higher temperatures are favorable for the products in endothermic reactions (e.g. H₂ and CO). With the increase of steam/biomass mass ratio, H₂ and CO₂ concentrations increase while CO concentration decreases. The carbon conversion decreases as the height of injection point increases owing to both an increase of solid entrainment and a decrease of particle residence time and particle temperature. Meanwhile, the calculated results compare well with the experimental data available in the literature. This indicates that the proposed CFD–DEM model and simulations are successful and it can play an important role in the multi-scale modeling of biomass gasification or combustion in fluidized bed reactor.

© 2014 Elsevier Ltd. All rights reserved.

1. Introduction

Due to the limited supply of conventional fossil fuels and global environmental problems, more and more attention has been paid to the renewable and clean energy technologies, among which biomass gasification is one of the most promising technologies for the efficient utilization of biomass. Biomass gasification is a complex thermo-chemical process in which biomass is converted into

synthetic gas (syngas), a combination of hydrogen, carbon monoxide, and methane. The syngas could be then used as a fuel in internal combustion engines, gas turbines, or fuel cells for the production of heat, mechanical energy, or power, or as a feedstock for the synthesis of liquid fuels and chemicals. The fundamental aspects of biomass gasification have been mainly studied by experiments using lab-scale reactors (Gil et al., 1999; Qin et al., 2012; Warnecke, 2000). Among the various gasification reactors, the fluidized bed (FB) reactor presents good prospects due to its high rates of heat and mass transfer, good temperature control, and its excellent mixing properties (Kern et al., 2013; Li et al., 2004; Shen et al., 2008). In a typical FB reactor, fuel feed, together with

* Corresponding author. Tel.: +47 73593919.

E-mail address: xiaoke.ku@ntnu.no (X. Ku).

inert bed material (e.g. sand) which acts as heat capacitance for the fuel, are fluidized by the gasifying agents, such as air (Kim et al., 2013), steam (Song et al., 2012), pure oxygen or their combination (Meng et al., 2011). There are many physico-chemical processes within a real biomass FB reactor, such as mixing, segregation, collision, particle heat-up, drying, pyrolysis, volatile matter combustion, and char reaction with O_2 /steam/ CO_2 . Moreover their scales are greatly separated, which results in detailed study of the entire gasification process being a challenging task.

Computational fluid dynamic (CFD) models have become more and more popular in recognizing the dense gas–solid flow dynamics (Lathouwers and Bellan, 2001; Papadikis et al., 2010; Ku et al., 2013) and chemical reactions (Ergüdenler et al., 1997; Nikoo and Mahinpey, 2008; Sadaka et al., 2002) in FB reactors. Generally, all the CFD models developed can be broadly categorized into Eulerian–Eulerian and Eulerian–Lagrangian approaches. For Eulerian–Eulerian approach, both particle and fluid phases are treated as interpenetrating continua. It can predict the macroscopic characteristics of a system with relatively low computational cost and has actually dominated the modeling of fluidization process for many years (Gerber et al., 2010; Taghipour et al., 2005; Wang et al., 2009). However, in addition to the difficulty of providing closure models for interaction terms between phases within its continuum framework, Eulerian–Eulerian approach does not recognize the discrete character of the particle phase and thus has trouble in modeling flows with a distribution of particle types and sizes. These difficulties can be naturally overcome by Eulerian–Lagrangian approach (Snider et al., 2011; Xie et al., 2013) in which the gas is treated as continuous and particle as discrete phase. When the particle phase is solved by discrete element method (DEM), the Eulerian–Lagrangian approach is also called CFD–DEM model. For CFD–DEM model, each particle is individually tracked and can be composed of multiple physical (size, density, composition, and temperature) and thermo-chemical (reactive or inert) properties. It can also offer detailed microscopic information at the particle level, such as particle trajectory, particle–particle and particle–fluid interaction, and transient forces acting on each particle, which is extremely difficult, even impossible to obtain by Eulerian–Eulerian approach. A crucial point when using CFD–DEM is the CPU load for particle collision monitoring as the number of particles increases. Thus, CFD–DEM simulations are often performed on the order of 10^4 particles and are mostly restricted to 2D or quasi-3D (domain width is one particle diameter) solutions. If chemical reactions are added, computation is more and more complicated and expensive. To date most of the CFD–DEM studies performed have been focused on the hydrodynamics of the isothermal fluidized bed and there have been few works on the simulation of dense gas–solid flow coupling with chemical reactions. Liu et al. (2011) used a CFD–DEM model to study char and propane combustion in a fluidized bed although their simulation conditions were strongly simplified, e.g., only 300 char particles were added at the start of simulation and there was no more fuel injection at later times. Bruchmüller et al. (2012) carried out a biomass fast pyrolysis simulation in a bubbling fluidized bed but did not take turbulence and chemical reactions into account. Gerber and Oevermann (2014) used a 2D CFD–DEM model to simulate wood gasification in a fluidized bed reactor but they used only charcoal as the bed material without any inert bed material such as sand used in ordinary experimental beds.

The aim of this study is to develop a comprehensive CFD–DEM model capable of describing dense, thermal, and reactive multiphase flows like biomass gasification in a fluidized bed reactor. The model described here is an extension of our previous hydrodynamic CFD–DEM model. In our earlier paper (Ku et al., 2013), an isothermal and non-reactive CFD–DEM model was developed and applied to a series of test cases in order to quantify its predictive

capabilities. These included (i) prediction of the characteristic fluidization behaviors (bubbles or slugs) of a typical bubbling fluidized bed, (ii) comparison of the minimum fluidization velocities predicted by different researchers, and (iii) comparison of the bed pressure drops generated by various drag correlations. The above comparisons performed have validated the hydrodynamic aspect of our CFD–DEM model. As a continuation, the hydrodynamic CFD–DEM model is enlarged here to account for the dense and reacting flows including models for turbulence, heat and mass transfer, radiation, particle shrinkage, pyrolysis, and heterogeneous and homogeneous reactions. The noteworthy novelties of the present CFD–DEM model include (i) a systematic presentation of the particle governing equations and gas transport equations within the Eulerian–Lagrangian concept, (ii) modeling of multiple homogeneous and heterogeneous reactions, (iii) resolving of turbulence by a k – ϵ model, (iv) 4×10^4 sand particles used as inert bed material and inter-particle and particle–wall collisions being resolved by a soft-sphere collision model, and (v) continuous biomass injection throughout the total simulation time. The integrated model is then applied to biomass gasification with steam in a lab-scale fluidized bed reactor. Simulation results are analyzed both qualitatively and quantitatively in terms of particle flow pattern, particle mixing and entrainment, bed pressure drop, composition distributions of product gas and other important characteristics in a fluidized bed reactor at different operating conditions (e.g. reactor temperature, steam/biomass mass ratio, biomass injection position). Besides, comparisons between calculated results and experimental data available in the literature are also carried out in order to verify the model.

This paper is organized as follows: In Section 2, the governing equations describing evolution of the particles and gas phase are firstly formulated. Herein, the sub-models of pyrolysis, char gasification, particle shrinkage, and gas phase reactions are also presented. In Section 3, the simulation setup is tabulated. In Section 4, the numerical results of biomass gasification with steam in a fluidized bed reactor are presented. Here, we first investigate the fluidization behavior, particle entrainment, and bed pressure drop. Then effects of different operating conditions, such as reactor temperature, steam/biomass mass ratio and biomass injection position, on the composition distributions of product gas and carbon conversion are documented where the CFD–DEM model is verified by comparing the calculated results with experimental data. Finally, a short summary and conclusions are given in Section 5. In addition, the symbols and subscripts used in the equations and abbreviations are described in the nomenclature at the end of the paper.

2. Mathematical modeling

The CFD–DEM model is formulated based on an unsteady-state Eulerian–Lagrangian multiphase model meaning transport equations are solved for the continuous gas phase and each of discrete particles is tracked through the calculated gas field. The interaction between the continuous phase and the discrete phase is taken into account by treating the exchange of mass, momentum and energy between the two systems as source terms in the governing equations. Specifically, the mechanisms of mass and energy exchange are adopted from the work of Kumar and Ghoniem (2012) with certain modifications as will be outlined below. Furthermore, for momentum exchange, detailed implementation issues are available in our earlier publication (Ku et al., 2013).

2.1. Discrete particle phase

The discrete particle phase consists of sand and biomass particles which are modeled in a Lagrangian manner. Sand plays

only the role of heat carrier in biomass gasification without taking part in any reactions, whereas biomass undergoes successive physical and chemical processes such as heat-up, drying, pyrolysis, and gasification and its behavior is strongly related to operating conditions.

2.1.1. Particle motion

The governing mass, momentum, and energy equations for each particle are as follows,

Mass:

$$\frac{dm_p}{dt} = \frac{dm_{\text{vapor}}}{dt} + \frac{dm_{\text{devol}}}{dt} + \frac{dm_{\text{C-CO}_2}}{dt} + \frac{dm_{\text{C-H}_2\text{O}}}{dt} \quad (1)$$

Momentum:

$$m_p \frac{d\mathbf{v}_p}{dt} = \mathbf{f}_g + \mathbf{f}_c + m_p \mathbf{g} \quad (2)$$

$$I_p \frac{d\boldsymbol{\omega}_p}{dt} = \mathbf{T}_p \quad (3)$$

$$\mathbf{f}_g = \frac{V_p \beta}{\varepsilon_p} (\mathbf{u}_g - \mathbf{v}_p) \quad (4)$$

$$\beta = \begin{cases} 150 \frac{\varepsilon_p^2 \mu_g}{\varepsilon_g d_p^2} + 1.75 \frac{\varepsilon_p \rho_g}{\varepsilon_g d_p} |\mathbf{u}_g - \mathbf{v}_p| & \varepsilon_g < 0.8 \\ \frac{3}{4} C_d \frac{\varepsilon_p \rho_g}{d_p} |\mathbf{u}_g - \mathbf{v}_p| \varepsilon_g^{-2.65} & \varepsilon_g \geq 0.8 \end{cases} \quad (5)$$

$$C_d = \begin{cases} \frac{24}{Re_p} (1 + 0.15 Re_p^{0.687}) & Re_p < 1000 \\ 0.44 & Re_p \geq 1000 \end{cases} \quad (6)$$

$$Re_p = \varepsilon_g \rho_g d_p |\mathbf{u}_g - \mathbf{v}_p| / \mu_g \quad (7)$$

Energy:

$$m_p c_p \frac{dT_p}{dt} = h A_p (T_g - T_p) + \frac{e_p A_p}{4} (G - 4\sigma T_p^4) + Q_p \quad (8)$$

As shown in Eq. (2), \mathbf{f}_c , i.e. the total contact force acting on particle due to inter-particle or particle-wall collisions, is taken into account and it is necessary for dense gas-particle flows. This is different from the model of Kumar and Ghoniem (2012) which does not consider the contact forces and thus their model is only applicable to dilute multiphase systems.

Here, the inter-phase momentum exchange coefficient β is modeled via the well-known Gidaspow drag correlation (Gidaspow, 1994). As shown in Eq. (5), the Gidaspow model combines Ergun (1952) and Wen and Yu (1966) correlations for the dilute and dense granular regime where a porosity ε_g of 0.8 is adopted as the boundary between these two regimes. This model is often used in the literature and effects of using different drag models were discussed in earlier publication (Ku et al., 2013).

As shown in Eq. (8), the particle temperature is calculated taking into account the heat transfer due to convection, radiation, and source term Q_p including both the latent heat of vaporization of water from the particle to the gas phase and the heat generated by the heterogeneous char reactions.

The inter-particle or particle-wall collisions are resolved by a soft-sphere discrete element method which was firstly proposed by Cundall and Strack (1979). In this method, the inter-particle contact forces are calculated using equivalent simple mechanical elements, such as spring, slider and dashpot (see Fig. 1). Particles are allowed to overlap slightly. The normal force tending to repulse the particles can then be deduced from this spatial overlap and the normal relative velocity at the contact point. The spring stiffness can be calculated by Hertzian contact theory when the physical properties such as Young's modulus and the Poisson ratio are known. A characteristic feature of the soft-sphere model is that

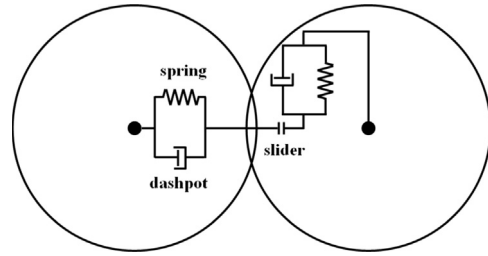
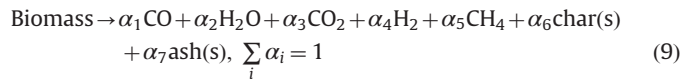


Fig. 1. The spring-slider-dashpot collision model.

it is capable of handling multiple particle-particle contacts which is of much importance when modeling dense particle systems like fluidized bed. Detailed implementation issues of the soft-sphere model are available in the literature (e.g. Tsuji et al., 1992), which are not stated here for the sake of shortness. In this study, the following physical properties are adopted for the collision model: Young's modulus is 5×10^6 Pa; Poisson ratio is 0.3; coefficient of restitution and friction coefficient are 0.9 and 0.3, respectively. All values are equally valid for walls and particles (Bruchmüller et al., 2012; Ku et al., 2013).

2.1.2. Pyrolysis

As soon as fresh biomass is fed into the bottom of the hot sand bed, it is immediately heated up, and thereby the devolatilization and pyrolysis of biomass as well as char gasification occurs. The pyrolysis compositions released from biomass can be expressed by the following equilibrium equation and each product yield is solved with the help of the elemental conservation analysis.



Note that, in the present model, reactions with sulfur and nitrogen are not taken into account due to their little amount (see Table 3), and they are considered passing directly to ash. CH_4 is the only hydrocarbon species taken into consideration. Although C_2H_2 , C_2H_4 , C_2H_6 , and other higher hydrocarbons (tar) are produced in the pyrolysis process, they are treated as non-stable products and this mechanism has also been widely used by other researchers (Ergüdenler et al., 1997; Gerber et al., 2010).

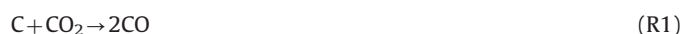
Consistent with Abani and Ghoniem's work (Abani and Ghoniem, 2013), the devolatilization rate is modeled using a single step first-order Arrhenius reaction.

$$\frac{dm_{\text{devol}}}{dt} = -A \exp\left(-\frac{E}{RT_p}\right) m_{\text{devol}} \quad (10)$$

where m_{devol} is the mass of the volatiles remaining in the particle, $A = 5.0 \times 10^6 \text{ s}^{-1}$, and $E = 1.2 \times 10^8 \text{ J/kmol}$ (Prakash and Karunanithi, 2008). The devolatilization process is assumed to be energetically neutral because the heat of devolatilization is generally negligible as compared to heat of reactions due to char consumption reactions (Abani and Ghoniem, 2013).

2.1.3. Char conversion chemistry

After devolatilization, the biomass particle is left with char and ash. Ash is assumed to be carried along with the particle without taking part in any reactions. Char will react in the presence of carbon dioxide and steam and gets converted into carbon monoxide and hydrogen. The following heterogeneous reactions are assumed and implemented in OpenFOAM.



Reactions R1 and R2 are endothermic gasification reactions and R1 is known as the Boudouard reaction.

The char consumption rate which includes the effects of both diffusion and kinetic rates is given as

$$\frac{dm_{C-i}}{dt} = -A_p p_i \frac{r_{diff,i} r_{kin,i}}{r_{diff,i} + r_{kin,i}} \quad (11)$$

$$r_{diff,i} = C_i \frac{[(T_p + T_g)/2]^{0.75}}{d_p} \quad (12)$$

$$r_{kin,i} = A_i T_p \exp\left(\frac{-E_i}{RT_p}\right) \quad (13)$$

where m_{C-i} is the mass of the char remaining in the particle when char reacts with gasifying species i ($=CO_2$, or H_2O), p_i is the partial pressure of the gasifying species, $r_{diff,i}$ and $r_{kin,i}$ are the diffusion rate and the kinetic rate, respectively. C_i is the mass diffusion rate constant. A_i and E_i are the parameters typical of the Arrhenius forms of kinetic rates. For wood biomass considered in the present study, the constants used for kinetic and diffusion rates are assembled below in Table 1 (Abani and Ghoniem, 2013).

2.1.4. Particle shrinkage

The char–gas chemistry consumes the solids and biomass particles shrink as they react with the gas phase. Particle shrinkage not only has an effect on gasification but also strongly affects particle trajectory on its way out of the reactor. Without particle shrinkage char entrainment will be highly over-predicted. Here we assume that particle density (ρ_p) stays constant throughout the gasification process and a mass-proportional shrinkage is adopted for each biomass particle. Thus the diameter of biomass particle shrinks as follows (Bruchmüller et al., 2012),

$$d_p = \left(\frac{6m_p}{\pi\rho_p}\right)^{1/3} \quad (14)$$

2.2. Continuous gas phase

The gas phase is modeled as a continuum, known as an Eulerian type model.

2.2.1. Gas phase motion

For continuum gas phase, the governing mass, momentum, energy, and species transport equations can be typically represented by the following equations.

Mass:

$$\frac{\partial}{\partial t}(\epsilon_g \rho_g) + \nabla \cdot (\epsilon_g \rho_g \mathbf{u}_g) = S_{p,m} \quad (15)$$

Momentum:

$$\frac{\partial}{\partial t}(\epsilon_g \rho_g \mathbf{u}_g) + \nabla \cdot (\epsilon_g \rho_g \mathbf{u}_g \mathbf{u}_g) = -\nabla p + \nabla \cdot (\epsilon_g \boldsymbol{\tau}_{eff}) + \epsilon_g \rho_g \mathbf{g} + S_{p,mom} \quad (16)$$

Energy:

$$\frac{\partial}{\partial t}(\epsilon_g \rho_g E) + \nabla \cdot (\epsilon_g \rho_g (\rho_g E + p)) = \nabla \cdot (\epsilon_g \alpha_{eff} \nabla h_s) + S_h + S_{p,h} + S_{rad} \quad (17)$$

$$E = h_s - \frac{p}{\rho_g} + \frac{u_g^2}{2} \quad (18)$$

Species:

$$\frac{\partial}{\partial t}(\epsilon_g \rho_g Y_i) + \nabla \cdot (\epsilon_g \rho_g \mathbf{u}_g Y_i) = \nabla \cdot (\epsilon_g \rho_g D_{eff} \nabla Y_i) + S_{p,Y_i} + S_{Y_i} \quad (19)$$

Note that the above transport equations have taken the volume fraction of gas ϵ_g into account and are applicable to the dense and reactive gas–particle flow in fluidized beds studied in this paper. They are different from the ones of Kumar and Ghoniem (2012) which do not consider ϵ_g and are only suitable for very dilute gas–particle flows.

Here, the effective stress tensor, $\boldsymbol{\tau}_{eff}$, is the sum of the viscous and turbulent stresses. Similarly the effective dynamic thermal diffusivity α_{eff} and mass diffusion coefficient for species D_{eff} take both the viscous and turbulent contributions into account. P-1 radiation model is adopted to solve the radiation source term S_{rad} as it has generally been chosen in CFD simulations of pulverized fuel gasification with radiation scattering (Backreedy et al., 2006).

As shown by Eq. (19), a transport equation is solved for each gas species, and the total gas phase properties are calculated from the mass fractions of the gas species making up the gas mixture. The mass, momentum, and enthalpy Eqs. (15), (16) and (17), respectively, are solved at each time step for the gas mixture. The flow is compressible, and the gas phase pressure, volume, temperature, and density are related through equations of state.

In order to solve turbulence, the governing transport equations for k and ϵ , which take into account the volume fraction of gas ϵ_g and are suitable for our dense gas–particle simulation system, are as follows (Kumar and Ghoniem, 2012; Wang et al., 2009),

$$\frac{\partial}{\partial t}(\epsilon_g \rho_g k) + \nabla \cdot (\epsilon_g \rho_g \mathbf{u}_g k) = \nabla \cdot \left(\epsilon_g \left(\mu_g + \frac{\mu_t}{\sigma_k} \right) \nabla k \right) + \epsilon_g G_k - \epsilon_g \rho_g \epsilon \quad (20)$$

$$\frac{\partial}{\partial t}(\epsilon_g \rho_g \epsilon) + \nabla \cdot (\epsilon_g \rho_g \mathbf{u}_g \epsilon) = \nabla \cdot \left(\epsilon_g \left(\mu_g + \frac{\mu_t}{\sigma_\epsilon} \right) \nabla \epsilon \right) + \epsilon_g \frac{\epsilon}{k} (C_{\epsilon 1} G_k - C_{\epsilon 2} \rho_g \epsilon) \quad (21)$$

The constants $C_{\epsilon 1}=1.44$, $C_{\epsilon 2}=1.92$, $\sigma_k=1.0$, and $\sigma_\epsilon=1.3$. The turbulent viscosity μ_t is computed as a function of k and ϵ ,

$$\mu_t = \rho_g C_\mu \frac{k^2}{\epsilon} \quad (22)$$

where C_μ is a constant which is set as 0.09.

2.2.2. Gas phase reactions

There are hundreds of gas phase chemical reactions in a gasification reactor. Even if all the elemental reactions and their rates of reaction could be identified, it is not possible to calculate so large number of coupled reactions. For the sake of simplification, a reduced set of 2 global reactions (3 reactions considering reverse reaction) is used to describe the major conversion rates in the reactor and effect of turbulence on reactions is resolved by the partially stirred reactor (PaSR) model (Abani and Ghoniem, 2013). Chemical reaction equations and their reaction rates as well as adopted references are listed in Table 2. The reaction rate is in $\text{kmol}/(\text{m}^3 \text{ s})$, and $[\cdot]$ implies mole concentration (kmol/m^3) of the gas species enclosed in the brackets. Reaction R3 is the consumption of CH_4 through steam reforming. Reaction R4 is known as the reversible water–gas shift reaction. Both forward reaction rate k_f

Table 1
Heterogeneous reaction constants.

Parameters	Values
A_{H_2O} (s/(m K))	45.6
E_{H_2O} (J/kmol)	4.37×10^7
A_{CO_2} (s/(m K))	8.3
E_{CO_2} (J/kmol)	4.37×10^7
C_i ($i=H_2O, CO_2$) (s/ $K^{0.75}$)	5.0×10^{-12}

Table 2

Considered homogeneous chemical reactions and their reaction rates.

Reactions		Reaction rate	Refs.
$\text{CH}_4 + \text{H}_2\text{O} \rightarrow \text{CO} + 3\text{H}_2$	(R3)	$k = 3.0 \times 10^8 [\text{CH}_4][\text{H}_2\text{O}] \exp(-1.26 \times 10^8 / RT)$	Jones and Lindstedt (1988)
$\text{CO} + \text{H}_2\text{O} \leftrightarrow \text{CO}_2 + \text{H}_2$	(R4)	$k_f = 2.78 \times 10^3 [\text{CO}][\text{H}_2\text{O}] \exp(-1.26 \times 10^7 / RT)$	Gómez-Barea and Leckner (2010)
		$k_b = 9.59 \times 10^4 [\text{CO}_2][\text{H}_2] \exp(-4.66 \times 10^7 / RT)$	
		$k_{\text{eq}} = 0.029 \exp(3.40 \times 10^7 / RT)$	

and reverse reaction rate k_b of R4 are calculated in lieu of a combined forward–reverse rate and k_f and k_b are related by the equilibrium constant $k_{\text{eq}} = k_f/k_b$.

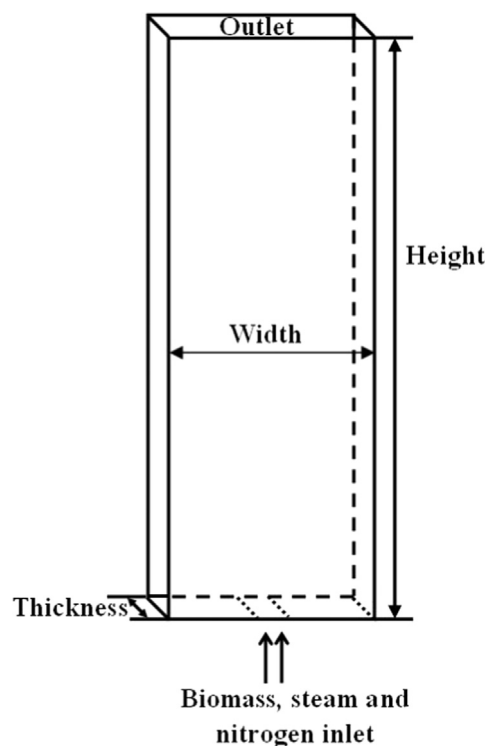
2.3. Computational methodology

Since the governing equations for particles and the gas phase are different, different solution schemes have to be used. For discrete particles, a first-order Euler time integration scheme is used to solve the translational and rotational motions of particles. Inter-particle and particle–wall collisions are modeled by soft-sphere collision method (see Fig. 1), where the solution scheme is well documented in the literature (e.g. Tsuji et al., 1992). Meanwhile, the drying, pyrolysis, and gasification submodels update particle properties like temperature, diameter, composition, and heat capacity at each fluid time step. For continuous gas phase, time discretization of the transporting equations is based on an Euler scheme and spatial discretization uses a finite-volume technique. The coupling between the discrete particles and the gas phase is achieved by the inter-phase source terms ($S_{p,m}$, $S_{p,mom}$, $S_{p,h}$, S_{p,Y_i}), which are solved at every fluid time step. All mathematical models and schemes described above have been developed and implemented into an open source C++ toolbox OpenFOAM (OpenCFD Ltd, 2012). The codes are made parallel and each case shown in the following sections takes about 14 days running time on a 16-core Intel node to accomplish the 20 s real time of simulation.

3. Simulation setup

All calculations are performed on a lab-scale biomass fluidized bed reactor which is taken from the experimental study of Song et al. (2012). Fig. 2 shows a sketch of the simulated geometry. It consists of a rectangular container of dimensions 0.23 m (width) \times 1.5 m (height) \times 0.0015 m (thickness) with a orifice of 0.01 m in width at the center of the bottom wall. The left, right, bottom walls, the bottom orifice and the top outlet compose the whole calculation domain boundaries. Initially, the reactor is filled completely with N_2 and a packed sand bed which is composed of 40,000 spherical sand particles with a diameter of 1.5 mm. The initial temperature of the sand and the gas in the domain is set equal to the operating reactor temperature (T_r). Hence, although the sand bed is initially stationary, it is assumed that it has been preheated. At the bottom inlet, mass flow rates for gas and biomass are specified, respectively. At the walls, no-slip conditions are applied for the gas phase and the wall temperature is specified according to the operating reactor temperature. At the top outlet, the atmospheric pressure boundary condition is adopted and particles are allowed to exit the computational domain during the simulation, modeling a fine solids entrainment phenomenon.

In the simulations, biomass is fed through the bottom orifice, together with a mixture of steam and nitrogen which is used as the gasifying agent as well as the fluidizing gas. The initial

**Fig. 2.** Geometry of the fluidized bed reactor.**Table 3**

Pine wood properties (Song et al., 2012).

Proximate analysis (wt%, on the as-received basis)		Elemental analysis (wt%, on the daf basis)	
Moisture	11.89	C	46.29
Ash	1.56	H	6.48
Volatile	71.78	O	46.08
Fixed carbon	14.77	N&S	1.15

diameter of biomass particle is 1.5 mm which is taken from the experiment. Pine wood is used as the biomass fuel and its initial properties, such as proximate and elemental analyses, are given in Table 3. The operating conditions such as reactor temperatures (T_r), biomass feed rate, and steam/biomass mass ratio (S/B), are in accordance with Song et al.'s (2012) experiment data. Table 4 summarizes the parameter settings used in the simulation and the boundary conditions for the gas phase are listed in Table 5. Note that all simulation cases are performed with a bottom biomass injection (see Fig. 2) except in Subsection 4.6. "Effect of biomass

Table 4

Parameter settings for the simulation system.

Property	Value	Property	Value
Bed size, (m)	$0.23 \times 1.5 \times 0.0015$	Sand density, (kg/m ³)	2600
Reactor temperature, (°C)	820, 870, 920	Sand specific heat, (J/(kg K))	860
CFD cell size, (m)	$0.01 \times 0.02 \times 0.0015$	Sand number, (dimensionless)	40,000
Fluid time step, (s)	1.0×10^{-5}	Biomass type, (dimensionless)	pine
Total simulation time, (s)	20	Initial biomass diameter, (mm)	1.5
Particle shape, (dimensionless)	Spherical	Biomass density, (kg/m ³)	470
Collision restitution coefficient, (dimensionless)	0.9	Biomass specific heat, (J/(kg K))	1500
Particle friction coefficient, (dimensionless)	0.3	Biomass feed rate, (g/s)	0.03125
Solid emissivity, (dimensionless)	0.9	Gas density, ρ_g	*
Sand diameter, (mm)	1.5	Inlet gas flow rate, (g/s)	0.18935

* ρ_g is determined based on the gas equation of state.**Table 5**

Boundary conditions for gas phase in the simulation.

Boundaries	Velocity	Pressure	Temperature	Porosity
Left and right walls	No slip	Zero gradient	Fixed value	Zero gradient
Bottom wall	No slip	Zero gradient	Zero gradient	Zero gradient
Inlet orifice (bottom)	Fixed flow rate	Zero gradient	Fixed value	Fixed value
Outlet (top)	Zero gradient	Fixed value	Zero gradient	Zero gradient

injection position” where the particle behaviors are compared among three different injection positions.

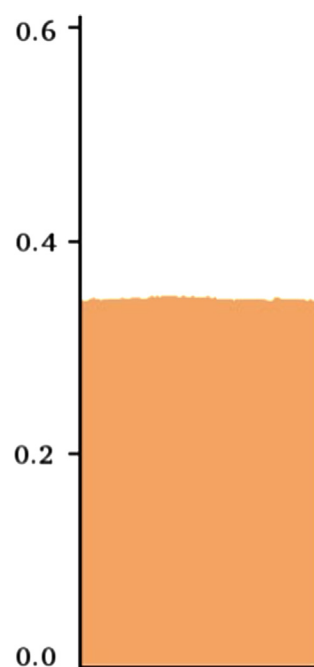
4. Results and discussions

4.1. Initial bed preparation

As described in Section 3, an initial packed sand bed is needed to start the fluidized bed simulation and it is generated as follows. The container is uniformly divided into a set of small rectangular lattices throughout the calculation domain. Then 40,000 sand particles with zero velocity are positioned at the centers of these lattices and allowed to fall down under the influence of gravity in the absence of inlet jet gas. As shown in Fig. 3, pluvial deposition of the particles finally results in a static bed of height about 0.35 m and porosity around 0.42. This deposited bed is then used as the initial packed bed for the fluidized bed gasification simulation. As pointed out by Xu and Yu (1997), the initial input data for this deposited bed include not only the particle coordinates but also the forces and torques which come with the deposition of particles in the packing process.

4.2. Fluidization behavior

To investigate the fluidization behavior of the bed, the formation and development of bubbles with time are firstly illustrated. Fig. 4 shows the simulated particle flow patterns with the time increment being 0.1 s at the beginning of simulation, representative for the base case ($T_r=820$ °C, $S/B=1.2$). Particles are colored by solid type. Brown color indicates sand particle and black color denotes biomass. Overall, the conditions in the reactor are almost symmetrical at the beginning of simulation. As an initial response of the bed to the introduction of fluidizing gas, a significant upward flow of particles is caused due to the instantaneous breakup of the inter-particle locking. It is readily observed that a big bubble (void structure) with an oval shape is firstly formed at the jet region ($t=0.1$ s), which forces particles in its front to rise. This bubble grows as gas flows upward and eventually collapses ($t=0.2$ s, 0.3 s). At later times, new bubbles continue to form at the bottom of bed and then they undergo the same procedure. Besides

**Fig. 3.** Particle configurations after a simulated packing process.

the bubble formation, the existence of “slug” structure at the upper part of the bed is also clearly predicted ($t=0.4$ s). The term “slug” is used here to describe a dilute region of particles which occupies the whole width of the bed and a similar definition is also given by other investigators (Hoomans et al., 1996; Kafui et al., 2002). The formation of bubbles and slugs in a typical fluidized bed reactor was also reported in the literature both numerically (Boyalakuntla, 2003; Hoomans et al., 1996; Xu and Yu, 1997) and experimentally (Tsuji et al., 1993). At $t=0.40$ s, a bed expansion estimated at 120% of the initial bed height is observed. Fig. 4 also shows the biomass particles (in black color), which start to enter into the reactor at $t=0$ through the bottom orifice, move up inside the dense sand bed.

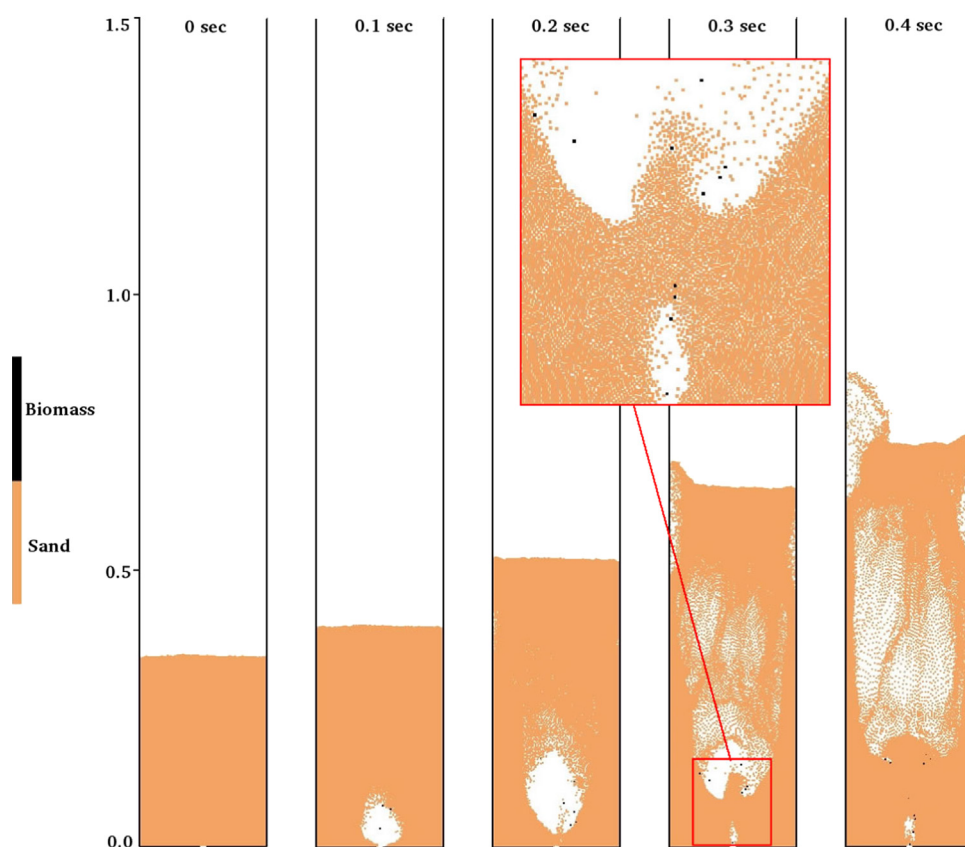


Fig. 4. Particle flow patterns with the time increment being 0.1 s at the beginning of simulation. $T_r=820\text{ }^{\circ}\text{C}$, $S/B=1.2$. (For interpretation of the references to color in this figure the reader is referred to the web version of this article.)

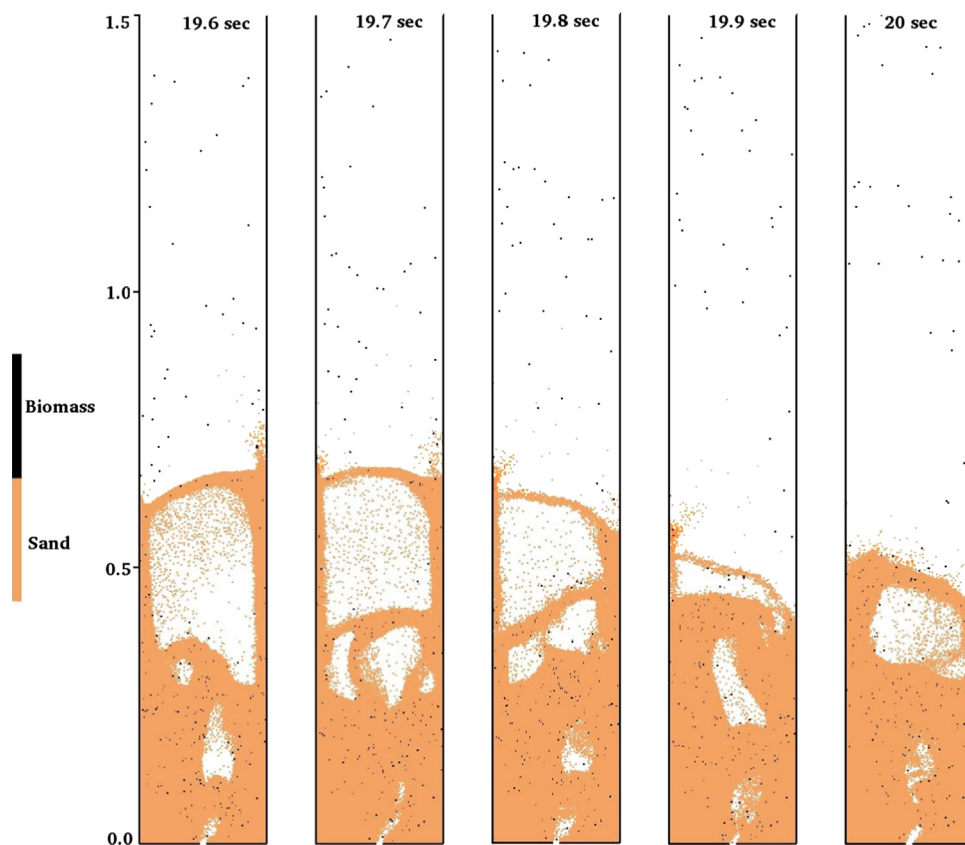


Fig. 5. Particle flow patterns with the time increment being 0.1 s at the end of simulation. $T_r=820\text{ }^{\circ}\text{C}$, $S/B=1.2$.

Fig. 5 depicts the particle flow patterns with the time increment being 0.1 s at the end of simulation. Generally, due to the gas productions from biomass by pyrolysis and gasification, the conditions in the reactor are not symmetrical and the bed is in a churned-turbulent state. It is observed that the inlet jet degenerates into bubbles, which rise through the bed and grow by coalescence with other bubbles to form slugs. When bubbles and slugs burst at the bed surface, particles tend to be pushed towards the wall and then fall down along the wall. This provokes a quite vigorous fluidization and strong mixing takes place. It is easily seen that biomass particles are relatively evenly distributed throughout the dense sand bed, illustrating the effectiveness for particle mixing which is regarded as a special characteristic of fluidized beds. Good mixing favors the direct contact between virgin cold biomass and hot sand and in turn allows a good heat transfer.

Fig. 6 depicts the snapshot of particle temperatures at the end of simulation. It is easily observed that the sand particles play the role of heat carrier and they have a temperature which is very close to the operating temperature ($T_r=820^\circ\text{C}$). At the same time, the strong mixing demonstrated in Fig. 5 favors the direct contact between virgin cold biomass and hot sand and results in a quick increase in the biomass temperature, whereas most of the biomass particles still have a relatively lower temperature compared to sand particles as shown in Fig. 6.

To show the transient behavior due to the fluidization of the bed, the pressure drop across the bed Δp is plotted in Fig. 7 as a function of time t . Δp is obtained as the difference between the average gas pressure in the bottom and top rows of the computational cells. It is easily observed that Δp fluctuates with time. The bed pressure drop fluctuations in a bubbling fluidized bed are considered to be caused by bubbles and slugs that form and collapse at regular intervals (Boyalakuntla, 2003) and effects of different drag models on the bed pressure drop has been discussed in our earlier paper (Ku et al., 2013).

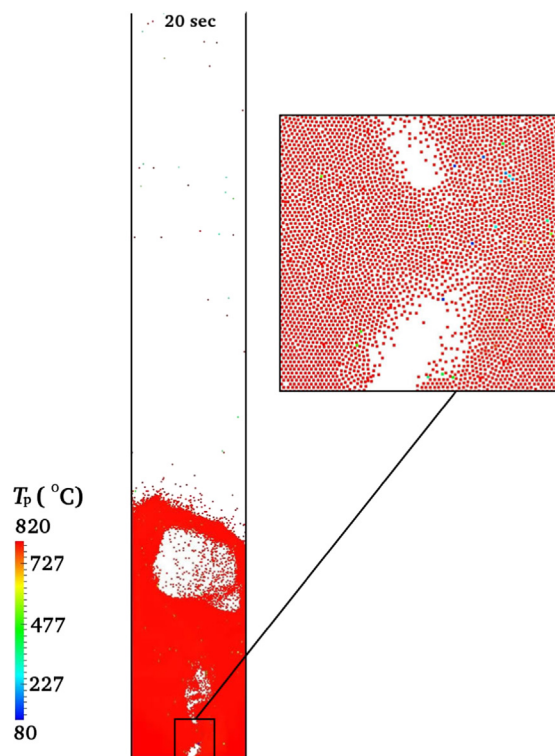


Fig. 6. Snapshot of particle temperatures at the end of simulation. $T_r=820^\circ\text{C}$, $S/B=1.2$.

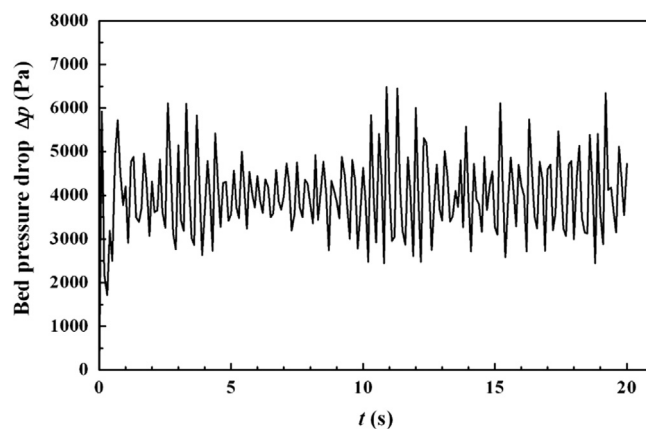


Fig. 7. Bed pressure drop Δp against time t . $T_r=820^\circ\text{C}$, $S/B=1.2$.

As shown in Figs. 4 and 5, the vigorous fluidization is characterized by the formation of large bubbles and slugs whose intensive eruptions can make light particles have high velocities and then reach the top outlet where they are eventually entrained out of the reactor (substantiated by snapshots at different times in Fig. 5). Fig. 8 shows the moving trajectory for a selected biomass particle before it is entrained. It is seen that, before entrainment occurs, the particle changes its moving direction and falls back (preferably near the wall) into the bed many times due to gas–particle interactions, particle–particle collisions and boundary effects near the bed top. This mechanism makes biomass particles have a long residence time in the reactor and a high carbon conversion ratio, which favors the syngas production from char gasification.

4.3. Product gas composition

For biomass gasification, H_2 and CO are the two most important product gas species. Figs. 9 and 10 illustrate the H_2 and CO mass fraction distributions in the reactor under base conditions ($T_r=820^\circ\text{C}$, $S/B=1.2$), respectively. It can be observed that, at the lower part of the reactor, the concentrations of H_2 and CO are high at similar locations representing regions where the biomass temperature has increased enough to produce large quantities of gas products due to devolatilization and gasification reactions. Moreover, the conditions in the reactor are not symmetrical which is also caused by the gas products from biomass by pyrolysis and gasification. From the analysis in the previous section, we know that, in a vigorous fluidized bed reactor, particles tend to migrate outwards toward the wall, driven by gas–particle interactions, particle–particle collisions and boundary effects, and then descend along the wall. As a result, there is a higher concentration of particles in the wall region where H_2 and CO concentrations are augmented as shown in Figs. 9 and 10. At the upper part of the reactor, the almost homogeneities in the mass fractions of H_2 and CO are a result of both the lower particle concentration and the gas transport process in the reactor.

Fig. 11 shows the volume fractions of the product gas compositions at the reactor outlet as a function of time t for the base case ($T_r=820^\circ\text{C}$, $S/B=1.2$). Note that the calculated results are based on the dry and N_2 free gas, which is consistent with the experimental study of Song et al. (2012). It is observed that there is only a strong dependence of product gas compositions on t in the initial period of simulation ($t < 5$ s). After the initial period ($t > 5$ s), each composition reaches a quasi-steady state. Thus in the following

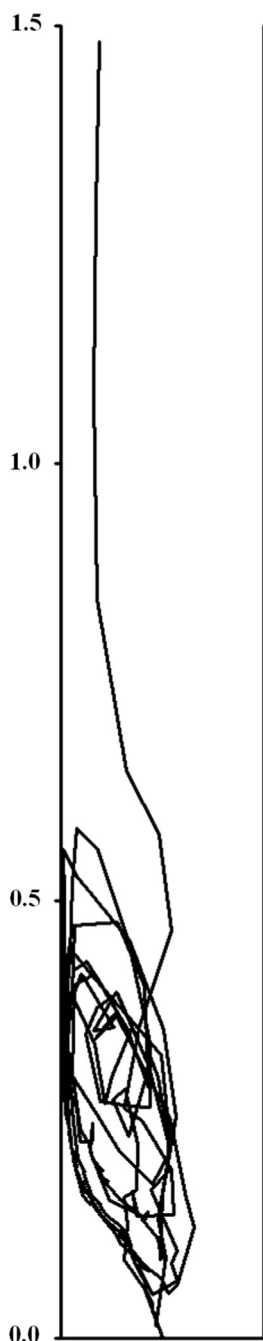


Fig. 8. Moving trajectory for a selected biomass particle before it is entrained out of the reactor. $T_r=820\text{ }^{\circ}\text{C}$, $S/B=1.2$.

sections, all the quantitative results are on a time-average basis from $t=5\text{ s}$ to 20 s .

4.4. Effect of reactor temperature

Operating reactor temperature (T_r) plays an important role in biomass gasification. Fig. 12 shows comparisons of the calculated results with the experimental data of Song et al. (2012) for product gas composition versus reactor temperature in the range of $820\text{--}920\text{ }^{\circ}\text{C}$. The steam/biomass mass ratio (S/B) is fixed at 1.2. It can be observed that, the predictions of the model show good conformance to the experimental measurements. For the two most important syngas species (H_2 , CO), the minimum relative error of calculation to experiment is about 1% and the maximum relative

error is less than 25%. For CO_2 , the maximum relative error is also within 30%. The underestimation of CH_4 can be attributed to the simplification of pyrolysis model and the neglect of tar and methanation reaction. Considering there exist no complete and unified set of gasifier chemistry equations and reaction rates in the open literature, errors cannot be avoided. This implies that the present CFD–DEM simulations are reasonable and the validity of the integrated model is verified.

The product gas composition is the result of the combination of a series of complex and competing reactions, as given in reactions (R1–R4). Generally speaking, higher temperature favors the products in endothermic reactions. Those endothermic reactions include the Boudouard (R1), the (R2) and the methane–steam reforming reaction (R3). Thus reactions (R1)–(R3) are strengthened with an increase in the reactor temperature, which result in an increase of CO and a decrease of CO_2 and CH_4 in the product gas. For H_2 , on the one hand, high temperature is in favor of H_2 formation owing to endothermic reactions (R2) and (R3). On the other hand, the temperature increase impels the exothermic water–gas shift reaction (R4) toward the negative direction at the expense of H_2 . Therefore, the trend of H_2 content with increasing temperature is governed by the competing reactions (R2)–(R4). As shown in Fig. 12, H_2 content slightly decreases with an increase in the reactor temperature for the experiment, while it is not very sensitive to the temperature change for the simulation.

4.5. Effect of steam/biomass mass ratio

The effect of steam/biomass mass ratio (S/B) on the product gas composition at the reactor temperature of $820\text{ }^{\circ}\text{C}$ is shown in Fig. 13. Again, the calculated exit gas compositions are in a good agreement with the experiment. With the increase of S/B , H_2 and CO_2 concentrations increase while CO concentration decreases. This can be mainly explained by water–gas shift reaction (R4) and high S/B boosts the forward reaction of (R4). Furthermore, due to methane–steam reforming reaction (R3), slightly decreasing trend of CH_4 composition with S/B is observed.

4.6. Effect of biomass injection position

Biomass injection position is another important parameter for design purposes. Fig. 14 shows the effect of three different injection points on the biomass particle distributions. For clarity purpose, the sand particles are excluded in the figure. As shown in Fig. 14, besides the default bottom feed point (Feed1), two other feed points, Feed2 and Feed3, are created at the left side wall and located at 0.2 m and 0.6 m above the bottom of the reactor, respectively. Feed2 denotes a point at the lower part of the sand bed and Feed3 represents a point just above or near the top of the sand bed. Therefore, the three feeding points adopted covers both bottom and top feeding of fuel which are commonly used in practical applications.

Fig. 14 shows that, for Feed1 and Feed2, no significant difference related to biomass particle distributions is observed except for a small local accumulation of biomass close to Feed2 position. However, for Feed3 where biomass is injected near the sand bed surface, the relatively low density of biomass precludes its good mixing with the sand bed and more biomass particles tend to be in the freeboard and then have a higher probability of being entrained out of the reactor.

Fig. 15 depicts the average biomass particle temperature for the three different injection points. Specifically, the values of particle temperature for the Feed1, Feed2, and Feed3 are $692.3\text{ }^{\circ}\text{C}$, $686.9\text{ }^{\circ}\text{C}$, and $661.3\text{ }^{\circ}\text{C}$, respectively. As expected, Feed1 has the highest biomass particle temperature due to its best mixing performance.

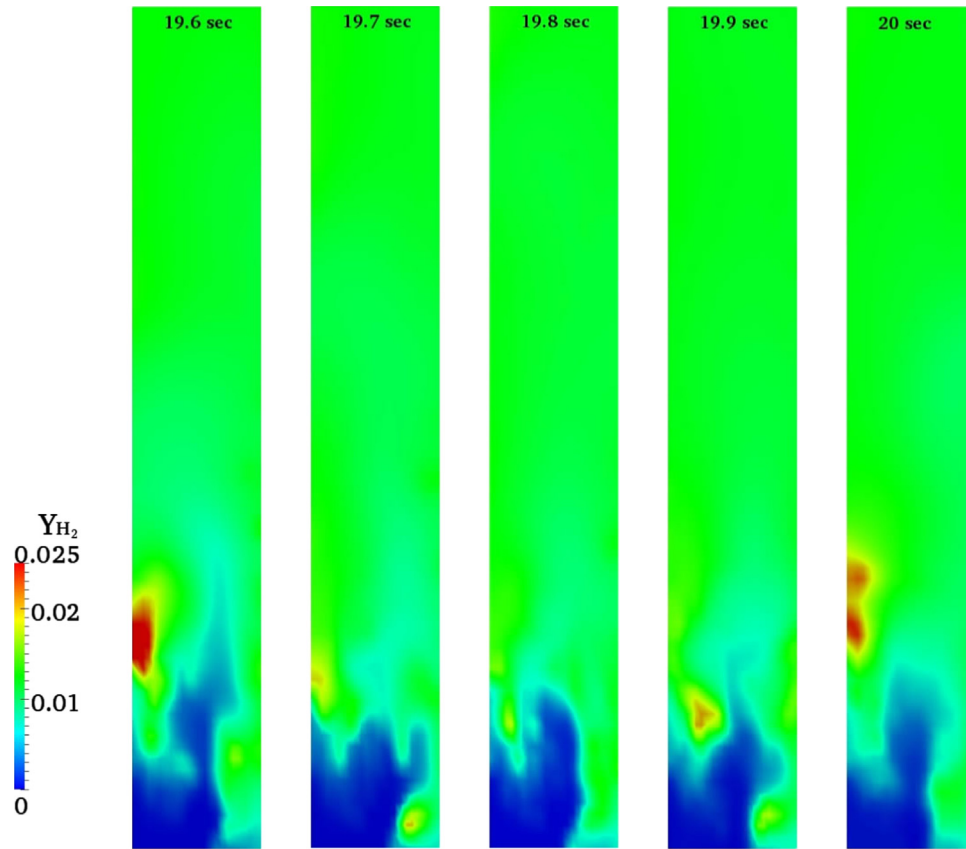


Fig. 9. Snapshots of H_2 mass fractions with the time increment being 0.1 s at the end of simulation. $T_r=820$ °C, $S/B=1.2$.

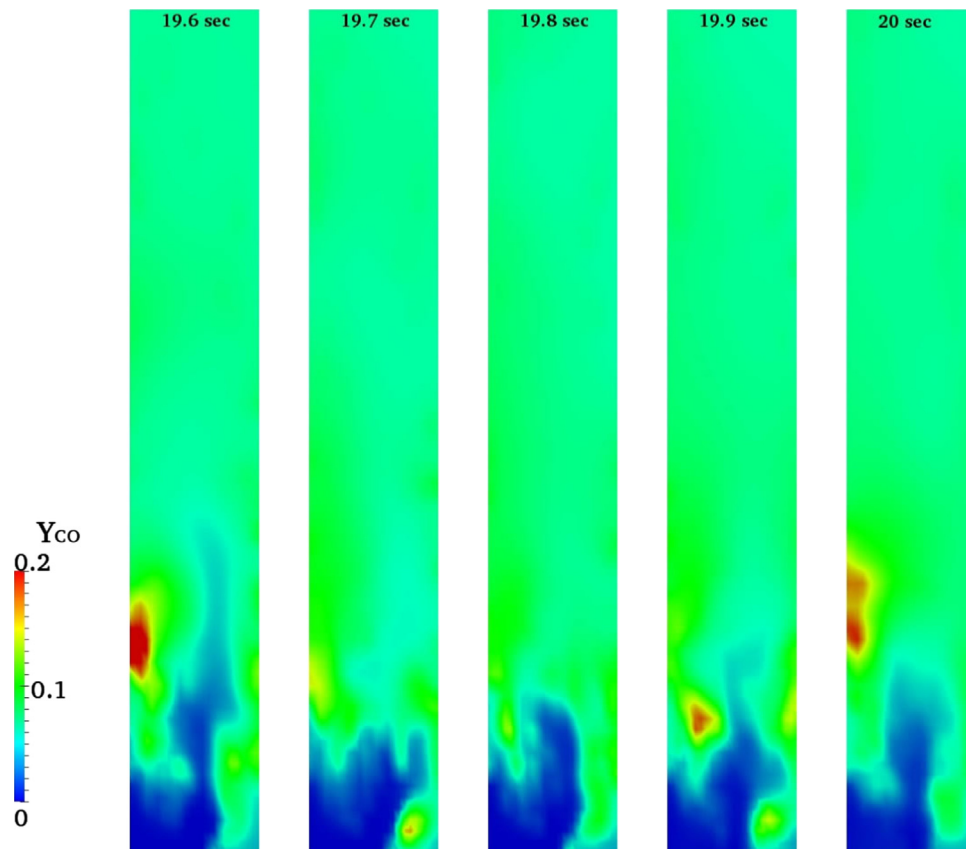


Fig. 10. Snapshots of CO mass fractions with the time increment being 0.1 s at the end of simulation. $T_r=820$ °C, $S/B=1.2$.

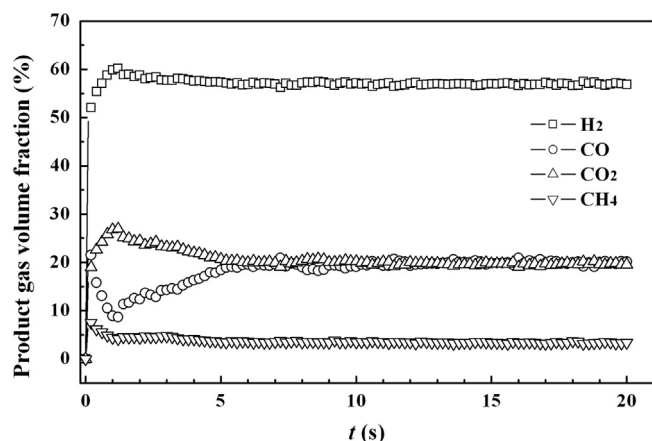


Fig. 11. Temporal evolution of product gas volume fractions at the reactor outlet. $T_r=820\text{ }^{\circ}\text{C}$, $S/B=1.2$.

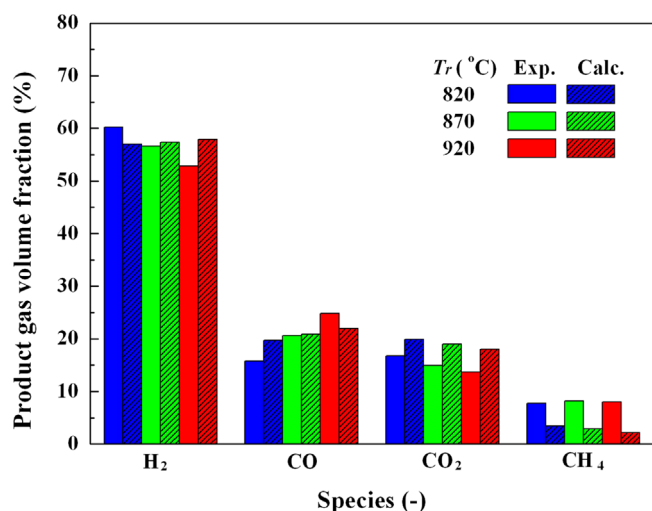


Fig. 12. Effect of reactor temperature on product gas composition at the reactor outlet. $S/B=1.2$.

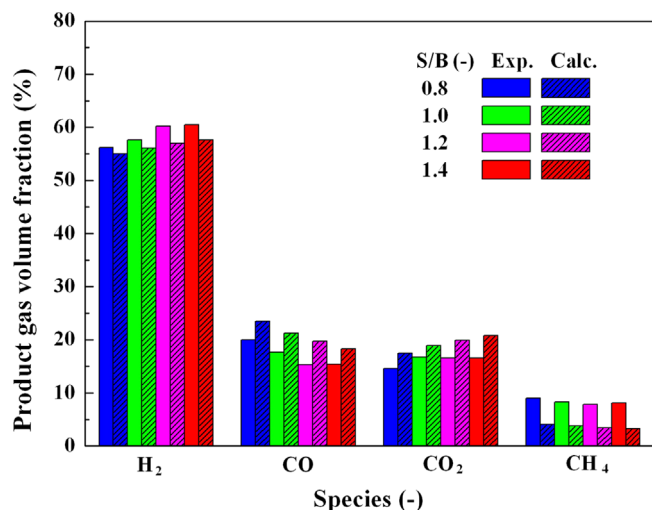


Fig. 13. Effect of steam/biomass mass ratio on product gas composition at the reactor outlet. $T_r=820\text{ }^{\circ}\text{C}$.

because the vaporization process occurs at a very fast rate due to the high operating temperature ($T_r=820\text{ }^{\circ}\text{C}$). Specifically, the values of moisture content for the Feed1, Feed2, and Feed3 are 0.07%, 0.10%, and 0.20%, respectively. Again, as expected, Feed3 has the highest moisture content due to its worst mixing performance which in turn results in a lowest biomass particle temperature as shown in Fig. 15.

Carbon conversion (CC) is a vital index used for evaluating the performance of gasification. It is defined as follows (Chen et al., 2013),

$$\text{CC (\%)} = \frac{\dot{m}_{\text{out,CO}} 12/28 + \dot{m}_{\text{out,CO}_2} 12/44 + \dot{m}_{\text{out,CH}_4} 12/16}{\dot{m}_{\text{in,fuel}} Y_c} \times 100 \quad (23)$$

where Y_c is the mass fraction of carbon in the feed fuel (biomass).

Fig. 17 shows the CC at the reactor outlet for the three injection points. Specifically, the values of CC for the Feed1, Feed2, and Feed3 are 95.3%, 94.9%, and 86.7%, respectively. The CC decreases as the height of injection point increases owing to both an increase of solid entrainment and a decrease of particle residence time and particle temperature (see Figs. 14 and 15).

5. Conclusions

A comprehensive CFD-DEM numerical model has been developed to simulate the biomass gasification process in a fluidized bed reactor. The gasifying agent is steam. The methodology is based on an Eulerian-Lagrangian concept, which uses an Eulerian method for gas phase and a discrete element method for particle phase. Each particle is individually tracked and associated with a range of physical and thermo-chemical properties, making it possible to look at accurate and detailed multi-scale information (i.e., any desired particle property, trajectory, and particle interaction) over the entire particle life time. The integrated model further considers particle collisions, hydrodynamics of dense gas-particle flow in fluidized beds, turbulence, heat and mass transfer, radiation, particle shrinkage, pyrolysis, as well as homogeneous and heterogeneous chemical reactions. The interaction between the continuous gas phase and the discrete particle phase is also considered by treating the exchange of mass, momentum and energy between the two systems as source terms in the governing equations.

Effects of different operating conditions, such as reactor temperature, steam/biomass mass ratio, and biomass injection position, on the gasification performance are analyzed. Simulation results are analyzed both qualitatively and quantitatively in terms of particle flow pattern, particle mixing and entrainment, bed pressure drop, product gas composition, and carbon conversion. Results show that higher temperatures are favorable for the products in endothermic reactions (e.g. H_2 and CO). With the increase of steam/biomass mass ratio, H_2 and CO_2 concentrations increase while CO concentration decreases. The carbon conversion decreases as the height of injection point increases owing to both an increase of solid entrainment and a decrease of particle residence time and particle temperature. Meanwhile, the integrated model has also been validated by comparing the calculated results with the experimental data. This indicates that the proposed CFD-DEM model can provide not only the macro structures at fluidized bed scale (bubble or slug) but also detailed microscopic information at the particle level (such as particle trajectory, particle-particle interaction, particle entrainment, and particle reaction, see Figs. 5, 8 and 14) which is impossible to obtain by an Eulerian-Eulerian approach. So our proposed model can be a powerful tool to gain an insight into the complex dense gas-particle flow behaviors and chemical reaction characteristics

Fig. 16 shows the average moisture content of biomass particles for the three different injection points. It can be seen that the moisture content is very low for all three injection positions

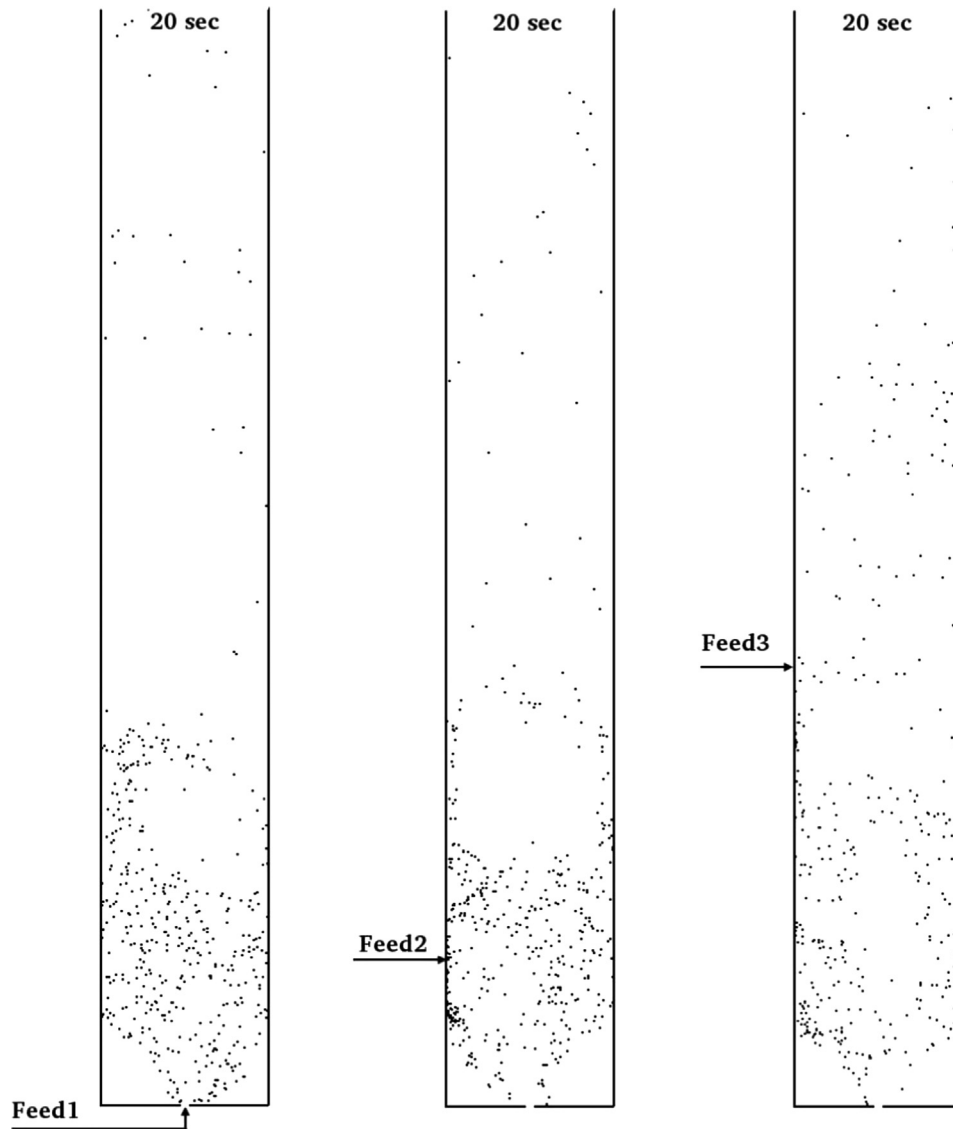


Fig. 14. Biomass particle distributions at the end of simulation for three different injection positions. Note that sand particles are excluded for clarity purpose. $T_r=820\text{ }^{\circ}\text{C}$, $S/B=1.2$.

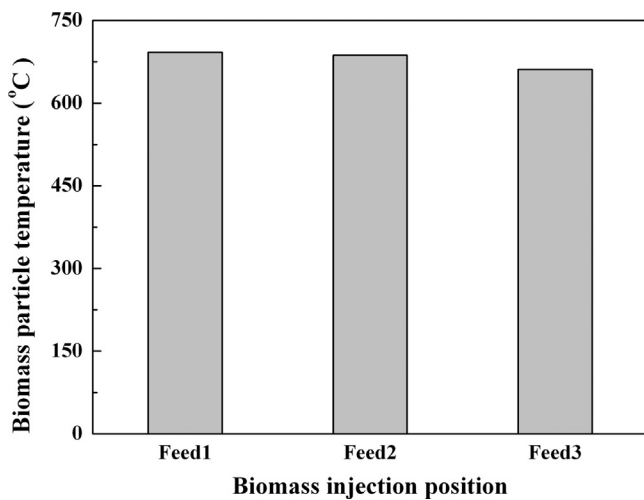


Fig. 15. Average biomass particle temperature for the three different injection positions. $T_r=820\text{ }^{\circ}\text{C}$, $S/B=1.2$.

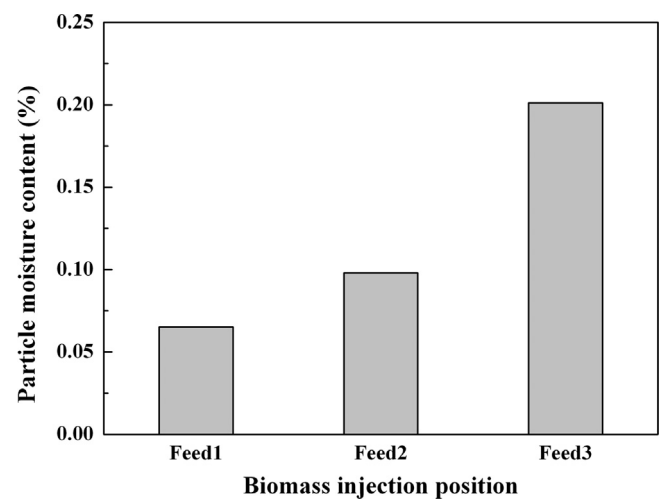


Fig. 16. Average moisture content of biomass particles for the three different injection positions. $T_r=820\text{ }^{\circ}\text{C}$, $S/B=1.2$.

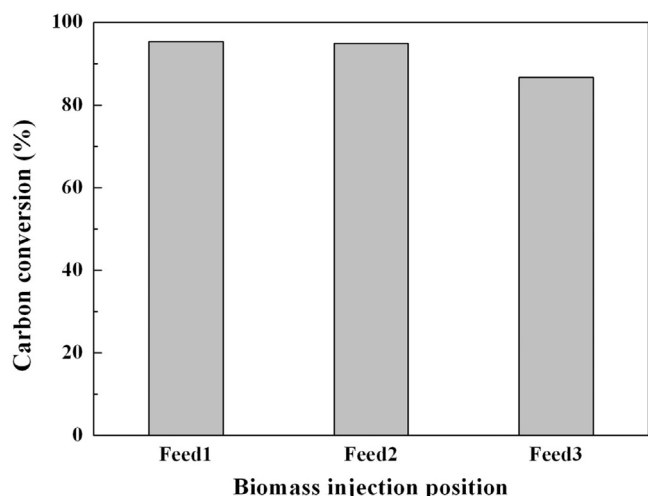


Fig. 17. Carbon conversion at the reactor outlet for the three different injection positions. $T_r = 820^\circ\text{C}$, $S/B = 1.2$.

simultaneously in the process of biomass gasification in a fluidized bed reactor.

Nomenclature

A	pre-exponential factor, 1/s
A_p	particle surface area, m^2
c_p	specific heat of particle, $\text{J}/(\text{kg K})$
C_d	drag coefficient, dimensionless
$C_{\varepsilon 1}, C_{\varepsilon 2}$	model constants for ε equation
d_p	particles diameter, m
dm_{C-H_2O}	change in mass of particle due to char reaction R2, kg
dm_{C-CO_2}	change in mass of particle due to char reaction R1, kg
dm_{devol}	change in mass of particle due to devolatilization, kg
dm_{vapor}	change in mass of particle due to loss of water vapor, kg
D_{eff}	effective mass diffusion coefficient for gas, m^2/s
e_p	particle emissivity, dimensionless
E	activation energy, J/kmol or parameter in Eq. (18), J/kg
\mathbf{f}_c	total contact force acting on particle due to collision, N
\mathbf{f}_g	gas drag force acting on particle, N
\mathbf{g}	gravitational acceleration, m/s^2
G	incident radiation, kg/s^3
G_k	generation term for k
h	heat transfer coefficient, $\text{W}/(\text{m}^2 \text{K})$
h_s	sensible enthalpy of gas phase, J/kg
I_p	moment of inertia of particle, kg m^2
k	reaction kinetics, $\text{kmol}/(\text{m}^3 \text{s})$ or turbulent kinetic energy, m^2/s^2
m_p	particle mass, kg
p	gas pressure, Pa
p_i	partial pressure of gas species i , Pa
Q_p	energy source term in particle energy equation, W
R	universal gas constant, $\text{J}/(\text{kmol K})$
Re_p	particle Reynolds number, dimensionless
S_h	enthalpy source term due to homogeneous reactions, W/m^3
$S_{p,m}$	mass source term from particle phase, $\text{kg}/(\text{m}^3 \text{s})$
$S_{p,h}$	enthalpy source term from particle phase, W/m^3
S_{rad}	radiation source term in gas phase energy equation, W/m^3
S_{p,Y_i}	species source term from particle phase, $\text{kg}/(\text{m}^3 \text{s})$
S_{Y_i}	species source term due to homogeneous reactions, $\text{kg}/(\text{m}^3 \text{s})$

$S_{p,mom}$	momentum source term, N/m^3
t	time, s
T_g	gas temperature, K
T_p	particle temperature, K
\mathbf{T}_p	torque acting on particle, $\text{kg m}^2/\text{s}^2$
\mathbf{u}_g	gas velocity, m/s
\mathbf{v}_p	particle velocity, m/s
V_p	particle volume, m^3
Y_i	mass fraction of species i , dimensionless

Greek letters

α_{eff}	effective thermal diffusivity, $\text{kg}/(\text{m s})$
β	inter-phase momentum exchange coefficient, $\text{kg}/(\text{m}^3 \text{s})$
ε	dissipation rate of turbulent kinetic energy, m^2/s^3
ε_g	volume fraction of gas, dimensionless
ε_p	volume fraction of particle, dimensionless
μ_g	gas phase viscosity, $\text{kg}/(\text{m s})$
μ_t	turbulent viscosity, $\text{kg}/(\text{m s})$
ρ_g	gas density, kg/m^3
ρ_p	particle density, kg/m^3
σ	Stefan–Boltzmann constant, $\text{W}/(\text{m}^2 \text{K}^4)$
σ_K	constant in Eq. (20)
σ_ε	constant in Eq. (21)
$\boldsymbol{\tau}_{\text{eff}}$	effective stress tensor, Pa
$\boldsymbol{\omega}_p$	particle angular velocity, 1/s

Subscripts

c	contact
g	gas phase
i	general index
p	particle
t	turbulent

Abbreviations

CC	carbon conversion
CFD	computational fluid dynamics
daf	dry and ash free
DEM	discrete element method
FB	fluidized bed
syngas	synthetic gas

Acknowledgments

The authors would like to thank partners in CenBio, the BioEnergy Innovation Centre, and GasBio for financial support.

References

- Abani, N., Ghoniem, A.F., 2013. Large eddy simulations of coal gasification in an entrained flow gasifier. *Fuel* 104, 664–680.
- Backreedy, R.I., Fletcher, L.M., Ma, L., Pourkashanian, M., Williams, A., 2006. Modelling pulverised coal combustion using a detailed coal combustion model. *Combust. Sci. Technol.* 178, 763–787.
- Boyalakuntla, D.S., 2003. Simulation of Granular and Gas–Solid Flows using Discrete Element Method (Ph.D. thesis). Carnegie Mellon University, Pittsburgh, Pennsylvania.
- Bruchmüller, J., van Wachem, B.G.M., Gu, S., Luo, K.H., Brown, R.C., 2012. Modeling the thermochemical degradation of biomass inside a fast pyrolysis fluidized bed reactor. *AIChE J.* 58 (10), 3030–3042.
- Chen, W., Chen, C., Hung, C., Shen, C., Hsu, H., 2013. A comparison of gasification phenomena among raw biomass, torrefied biomass and coal in an entrained-flow reactor. *Appl. Energy* 112, 421–430.

- Cundall, P.A., Strack, O.D.L., 1979. A discrete numerical model for granular assemblies. *Geotechnique* 29, 47–65.
- Ergun, S., 1952. Fluid flow through packed columns. *Chem. Eng. Prog.* 48, 89–94.
- Ergüdenler, A., Ghaly, A.E., Hamdullahpur, F., Al-Taweel, A.M., 1997. Mathematical modeling of a fluidized bed straw gasifier: Part I—model development. *Energy Source* 19, 1065–1084.
- Gerber, S., Behrendt, F., Oevermann, M., 2010. An Eulerian modeling approach of wood gasification in a bubbling fluidized bed reactor using char as bed material. *Fuel* 89, 2903–2917.
- Gerber, S., Oevermann, M., 2014. A two dimensional Euler–Lagrangian model of wood gasification in a charcoal bed – Part I: model description and base scenario. *Fuel* 115, 385–400.
- Gidaspow, D., 1994. *Multiphase Flow and Fluidization*. Academic Press, San Diego, USA.
- Gil, J., Corella, J., Aznar, M.P., Caballero, M.A., 1999. Biomass gasification in atmospheric and bubbling fluidized bed: effect of the type of gasifying agent on the product distribution. *Biomass Bioenergy* 17, 389–403.
- Gómez-Barea, A., Leckner, B., 2010. Modeling of biomass gasification in fluidized bed. *Prog. Energy Combust.* 36, 444–509.
- Hoomans, B.P.B., Kuipers, J.A.M., Briels, W.J., van Swaaij, W.P.M., 1996. Discrete particle simulation of bubble and slug formation in a two-dimensional gas fluidised bed: a hard-sphere approach. *Chem. Eng. Sci.* 51, 99–118.
- Jones, W.P., Lindstedt, R.P., 1988. Global reaction schemes for hydrocarbon combustion. *Combust. Flame* 73, 233–249.
- Kafui, K.D., Thornton, C., Adams, M.J., 2002. Discrete particle-continuum fluid modelling of gas–solid fluidised beds. *Chem. Eng. Sci.* 57, 2395–2410.
- Kern, S., Pfeifer, C., Hofbauer, H., 2013. Gasification of wood in a dual fluidized bed gasifier: influence of fuel feeding on process performance. *Chem. Eng. Sci.* 90, 284–298.
- Kim, Y.D., Yang, C.W., Kim, B.J., Kim, K.S., Lee, J.W., Moon, J.H., Yang, W., Yu, T.U., Lee, U.D., 2013. Air-blown gasification of woody biomass in a bubbling fluidized bed gasifier. *Appl. Energy* 112, 414–420.
- Ku, X., Li, T., Løvås, T., 2013. Influence of drag force correlations on periodic fluidization behavior in Eulerian–Lagrangian simulation of a bubbling fluidized bed. *Chem. Eng. Sci.* 95, 94–106.
- Kumar, M., Ghoniem, A.F., 2012. Multiphysics simulations of entrained flow gasification. Part II: constructing and validating the overall model. *Energy Fuels* 26, 464–479.
- Lathouwers, D., Bellan, J., 2001. Modeling of dense gas–solid reactive mixtures applied to biomass pyrolysis in a fluidized bed. *Int. J. Multiph. Flow* 27 (12), 2155–2187.
- Li, X.T., Grace, J.R., Lim, C.J., Watkinson, A.P., Chen, H.P., Kim, J.R., 2004. Biomass gasification in a circulating fluidized bed. *Biomass Bioenergy* 26, 171–193.
- Liu, D., Chen, X., Zhou, W., Zhao, C., 2011. Simulation of char and propane combustion in a fluidized bed by extending DEM–CFD approach. *Proc. Combust. Inst.* 33, 2701–2708.
- Meng, X., de Jong, W., Fu, N., Verkooyen, A.H.M., 2011. Biomass gasification in a 100 kWth steam-oxygen blown circulating fluidized bed gasifier: effects of operational conditions on product gas distribution and tar formation. *Biomass Bioenergy* 35, 2910–2924.
- Nikoo, M.B., Mahinpey, N., 2008. Simulation of biomass gasification in fluidized bed reactor using ASPEN PLUS. *Biomass Bioenergy* 32 (12), 1245–1254.
- OpenCFD Ltd., 2012. *OpenFOAM-The open source CFD toolbox-user guide (Version 2.1.1)* (<http://www.openfoam.org/docs/>).
- Papadikis, K., Gu, S., Bridgwater, A.V., 2010. A CFD approach on the effect of particle size on char entrainment in bubbling fluidised bed reactors. *Biomass Bioenergy* 34, 21–29.
- Prakash, N., Karunanithi, T., 2008. Kinetic modeling in biomass pyrolysis – a review. *J. Appl. Sci. Res.* 4 (12), 1627–1636.
- Qin, K., Jensen, P.A., Lin, W., Jensen, A.D., 2012. Biomass gasification behavior in an entrained flow reactor: gas product distribution and soot formation. *Energy Fuels* 26, 5992–6002.
- Sadaka, S.S., Ghaly, A.E., Sabbah, M.A., 2002. Two phase biomass air-steam gasification model for fluidized bed reactors: Part I—model development. *Biomass Bioenergy* 22, 439–462.
- Shen, L., Gao, Y., Xiao, J., 2008. Simulation of hydrogen production from biomass gasification in interconnected fluidized beds. *Biomass Bioenergy* 32, 120–127.
- Snider, D.M., Clark, S.M., O'Rourke, P.J., 2011. Eulerian–Lagrangian method for three-dimensional thermal reacting flow with application to coal gasifiers. *Chem. Eng. Sci.* 66, 1285–1295.
- Song, T., Wu, J., Shen, L., Xiao, J., 2012. Experimental investigation on hydrogen production from biomass gasification in interconnected fluidized beds. *Biomass Bioenergy* 36, 258–267.
- Taghipour, F., Ellis, N., Wong, C., 2005. Experimental and computational study of gas–solid fluidized bed hydrodynamics. *Chem. Eng. Sci.* 60, 6857–6867.
- Tsuji, Y., Kawaguchi, T., Tanaka, T., 1993. Discrete particle simulation of two-dimensional fluidized bed. *Powder Technol.* 77, 79–87.
- Tsuji, Y., Tanaka, T., Ishida, T., 1992. Lagrangian numerical simulation of plug flow of cohesionless particles in a horizontal pipe. *Powder Technol.* 71, 239–250.
- Wang, X., Jin, B., Zhong, W., 2009. Three-dimensional simulation of fluidized bed coal gasification. *Chem. Eng. Process.* 48, 695–705.
- Warnecke, R., 2000. Gasification of biomass: comparison of fixed bed and fluidized bed gasifier. *Biomass Bioenergy* 18, 489–497.
- Wen, C.Y., Yu, Y.H., 1966. *Mechanics of fluidization*. *Chem. Eng. Prog. Symp. Ser.* 62, 100–111.
- Xie, J., Zhong, W., Jin, B., Shao, Y., Huang, Y., 2013. Eulerian–Lagrangian method for three-dimensional simulation of fluidized bed coal gasification. *Adv. Powder Technol.* 24, 382–392.
- Xu, B.H., Yu, A.B., 1997. Numerical simulation of the gas–solid flow in a fluidized bed by combining discrete particle method with computational fluid dynamics. *Chem. Eng. Sci.* 52, 2785–2809.